

## RESEARCH ARTICLE

10.1002/2016JD025350

## Modulation of atmospheric rivers near Alaska and the U.S. West Coast by northeast Pacific height anomalies

Bryan D. Mundhenk<sup>1</sup>, Elizabeth A. Barnes<sup>1</sup>, Eric D. Maloney<sup>1</sup>, and Kyle M. Nardi<sup>1,2</sup><sup>1</sup>Department of Atmospheric Science, Colorado State University, Fort Collins, Colorado, USA, <sup>2</sup>Department of Mathematics, Temple University, Philadelphia, Pennsylvania, USA

## Key Points:

- Atmospheric rivers occur near Alaska and the U.S. West Coast with similar frequency, but with different seasonality
- Northeast Pacific height anomalies modulate atmospheric river activity over a range of time scales
- Rossby wave breaking links height anomalies and atmospheric river activity with broader North Pacific dynamics

## Supporting Information:

- Supporting Information S1

## Correspondence to:

B. Mundhenk,  
bryan.mundhenk@colostate.edu

## Citation:

Mundhenk, B. D., E. A. Barnes, E. D. Maloney, and K. M. Nardi (2016), Modulation of atmospheric rivers near Alaska and the U.S. West Coast by northeast Pacific height anomalies, *J. Geophys. Res. Atmos.*, 121, doi:10.1002/2016JD025350.

Received 12 MAY 2016

Accepted 21 OCT 2016

Accepted article online 31 OCT 2016

**Abstract** Atmospheric rivers (ARs) can cause wide-ranging impacts upon landfall at high northern latitudes, but comparatively little is known about the dynamics supporting these ARs in contrast to their midlatitude counterparts. Here ARs near the U.S. West Coast and the Gulf of Alaska during 1979–2015 are compared. ARs are found to occur in both regions with similar frequency, but with different seasonality. Composited atmospheric conditions from the NASA Modern-Era Retrospective Analysis for Research and Applications data set reveal that a broad height anomaly over the northeast Pacific is influential to AR activity in both regions. When a positive height anomaly exists over the northeast Pacific, AR activity is often deflected poleward toward Alaska, while the U.S. West Coast experiences a decrease in AR activity. The opposing relationship also applies; that is, AR activity is decreased near Alaska and increased along the U.S. West Coast in the presence of a negative height anomaly. Quantitatively, nearly 79% of Gulf of Alaska ARs are associated with a positive northeast Pacific height anomaly and 86% of U.S. West Coast ARs are associated with a negative anomaly. Results suggest that this relationship applies across a range of time scales, to include subseasonal and interannual, not just with respect to individual transient waves. Both ARs and height anomalies are found to be associated with Rossby wave breaking, thereby dynamically linking AR activity with broader North Pacific dynamics.

## 1. Introduction

Atmospheric rivers (ARs) are filamentary plumes of focused tropospheric water vapor transport that dominate the flux of water vapor into and within the extratropics [e.g., *Zhu and Newell*, 1998; *Ralph et al.*, 2004; *Neiman et al.*, 2008a]. Landfalling ARs may trigger weather extremes such as heavy rainfall and localized flooding [e.g., *Ralph et al.*, 2006; *Neiman et al.*, 2008b; *Smith et al.*, 2010; *Neiman et al.*, 2011; *Ralph and Dettinger*, 2012; *Warner et al.*, 2012] and influence periods of regional drought and/or precipitation abundance [e.g., *Neiman et al.*, 2008a; *Guan et al.*, 2012; *Dettinger et al.*, 2011; *Dettinger*, 2013]. Perhaps due to these wide-ranging impacts, ARs affecting the western coastline of the contiguous United States (U.S.) have been extensively studied [see *Rutz et al.*, 2014; *Payne and Magnusdottir*, 2014; *Jackson et al.*, 2016, and references therein].

In contrast to ARs making landfall along the U.S. West Coast, high-latitude ARs in the Pacific basin have received comparatively little attention. The most comprehensive work available addressing ARs near Alaska, for example, is a National Oceanic and Atmospheric Administration National Weather Service internal paper on heavy precipitation and flooding in Alaska [*Papineau and Holloway*, 2011]. That paper concluded that the majority of the surveyed rain-generated flooding events in Alaska resulted from landfalling ARs.

Peer-reviewed literature provides background regarding the latitudinal variability of AR characteristics [*Ralph et al.*, 2004] and the composite synoptic-scale signatures of ARs near western North America [*Neiman et al.*, 2008a; *Roberge et al.*, 2009]; however, such studies do not address the high-latitude ARs that will be evaluated in this work. Recently, *Guan and Waliser* [2015] provided a global climatology of ARs that included an assessment of the landfall frequency, seasonality, and variability of ARs from 18 years of reanalysis data. *Mundhenk et al.* [2016] also evaluated the climatology and variability of ARs but focused on the North Pacific basin and included a brief analysis of a subregion extending over southwestern Alaska. *Brands et al.* [2016] calculated boreal wintertime AR counts through the twentieth century in four reanalysis data sets for five regions along the North American west coast that included two regions bordering the Gulf of Alaska. They corroborated *Guan and Waliser* [2015] who found AR activity along much of the western coastline is correlated with the Pacific-North American teleconnection pattern, though the significance of the relationship varied

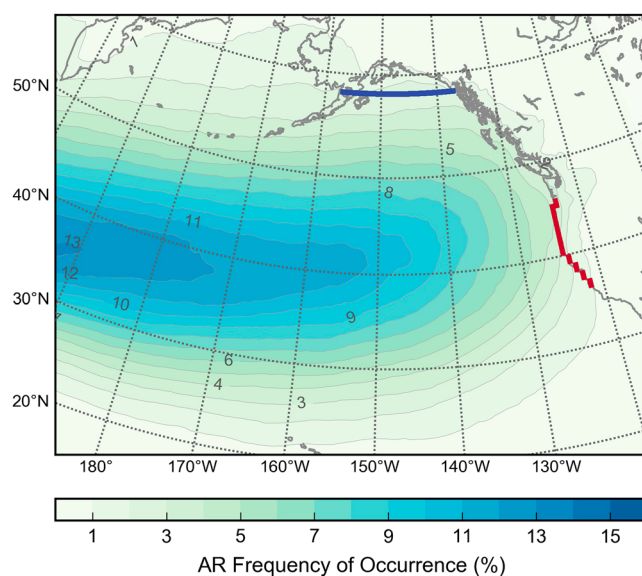


**Figure 1.** Location of the Gulf of Alaska (blue) and U.S. West Coast (red) landfall boundaries overlaying the annual mean AR frequency of occurrence (contoured shading).

that the most intense moisture intrusions into the Arctic occur when high pressure is positioned over the eastern Pacific. *Liu and Barnes* [2015] advanced the analysis of *Woods et al.* [2013] by documenting the link between synoptic-scale moisture transport into the Arctic across 60°N and Rossby wave breaking. They found that a substantial fraction of the extreme moisture intrusions into the Arctic are closely related to Rossby wave breaking. More recently, *Woods and Caballero* [2016] corroborated these and other works relating poleward moisture flux into the Arctic with midlatitude dynamics and variability. Motivated by these studies, we will examine the relationship between ARs and Rossby wave breaking in section 5.

Despite the limited mention of high-latitude ARs in the literature, they constitute a worthy and timely topic of investigation. Not only do high-latitude ARs cause notable impacts upon landfall [*Papineau and Holloway*, 2011, 2012], but AR-like features may also be responsible for the majority of the moisture flux into the Arctic [e.g., *Woods et al.*, 2013; *Liu and Barnes*, 2015; *Dufour et al.*, 2016] and may contribute to the Arctic amplification [e.g., *Woods and Caballero*, 2016]. Understanding these features and their resulting radiative effects and precipitation impacts is important for characterizing the climatology and variability of weather and climate at high latitudes.

In this work, we will analyze ARs that pass over the two distinct boundaries approximating landfall plotted in Figure 1, referred to as “Gulf of Alaska” (blue) and “U.S. West Coast” (red). The purpose of this study is threefold: (1) to compare and contrast the occurrence and attributes of ARs near southern Alaska with the comparatively well-documented ARs near the U.S. West Coast, (2) to assess the common meteorological conditions associated with these ARs and the differences between them, and (3) to investigate the large-scale atmospheric dynamics that may explain the variability of AR activity at synoptic, subseasonal, and interannual time scales.

The remainder of this manuscript is organized into five sections. Section 2 includes a brief description of the data sets and methods used in this work. Section 3 compares and contrasts the occurrence and attributes of ARs over the two landfall boundaries. Section 4 assesses the relationship between the large-scale atmospheric conditions and AR activity at the synoptic, subseasonal, and interannual time scales. Section 5 explores the related dynamics. Finally, the study’s results are concluded in section 6.

## 2. Data and Methods

### 2.1. Atmospheric Variables

The National Aeronautics and Space Administration (NASA) Modern-Era Retrospective Analysis for Research and Applications (MERRA) reanalysis data set [*Rienecker et al.*, 2011] is the source for all of the atmospheric variables analyzed in this work. Unless specified otherwise, 37 years (1979–2015) of instantaneous data at

based on the season and particular reanalysis data set. *Brands et al.* [2016] also found seasonal AR counts near British Columbia and the Gulf of Alaska to be correlated with the strength of the climatological Aleutian low. None of these works methodically explored the atmospheric dynamics associated with high-latitude ARs over the North Pacific, and so we address this knowledge gap in sections 3–5 of this manuscript.

Recent research into the dynamics supporting poleward moisture fluxes into the Arctic provides a framework for our research in terms of actual ARs and their connection with the large-scale dynamics of the North Pacific. For example, *Woods et al.* [2013] investigated the broad circulation patterns associated with wintertime transport of moisture across 70°N. They found

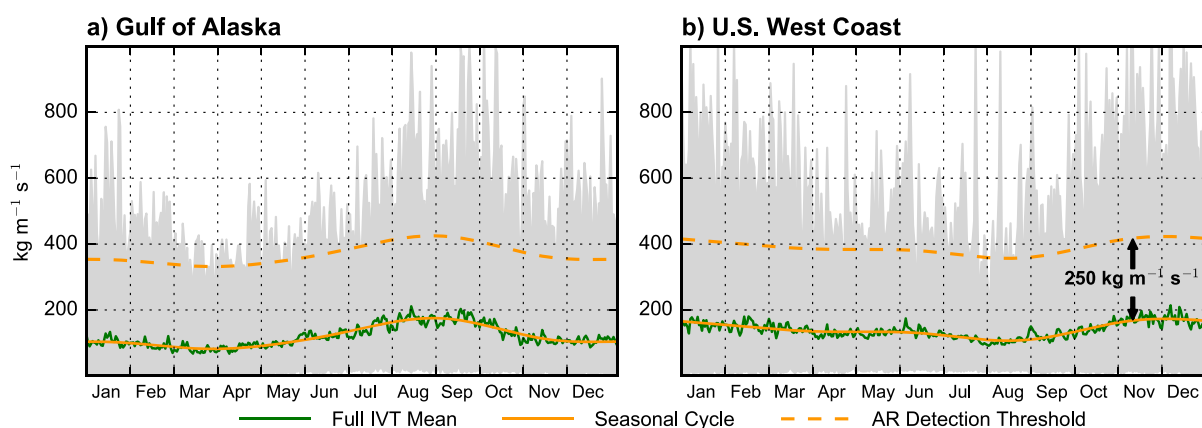


**Figure 2.** Comparison of IVT values and the AR detection threshold along the (a) Gulf of Alaska and (b) U.S. West Coast landfall boundaries. In each panel, the seasonal cycle of IVT (solid orange curve) and the AR detection threshold (dashed orange curve) overlay the daily maximum/minimum range of IVT values from the 37 year record (gray shading) and the daily mean IVT (solid green curve).

6-hourly temporal resolution and native spatial resolution ( $\frac{1}{2}^{\circ}$  latitude  $\times$   $\frac{2}{3}^{\circ}$  longitude) on isobaric surfaces are used.

## 2.2. Atmospheric Rivers

ARs are objectively identified using the detection algorithm described in *Mundhenk et al.* [2016]. The algorithm uses fields of positive anomalous, instantaneous vertically integrated water vapor transport (IVT'), calculated from MERRA reanalysis data spanning 1000 to 300 hPa, together with a series of intensity and geometric (e.g., total area, length, and length-to-width ratio) criteria, to detect AR-like features. As noted in *Mundhenk et al.* [2016], the use of anomalies aids automated feature detection in large spatial domains and across all seasons and allows for the use of a static  $250 \text{ kg m}^{-1} \text{ s}^{-1}$  IVT' threshold within the detection scheme. Although the actual detection threshold does not vary in the algorithm, the comparable, or equivalent, full IVT threshold (i.e., mean and seasonal cycle *not* removed) varies spatially and temporally, as evidenced by Figure 2. The detection threshold, shown by the dashed orange curves, follows the seasonal cycle of IVT in both regions and appears suitable for the year-round detection of ARs for both of the landfall boundaries in this analysis. Furthermore, the  $250 \text{ kg m}^{-1} \text{ s}^{-1}$  IVT' threshold should not be considered as equivalent to a  $250 \text{ kg m}^{-1} \text{ s}^{-1}$  threshold for full IVT that one may encounter in other detection schemes [e.g., *Rutz et al.*, 2014; *Radić et al.*, 2015].

The AR detection algorithm employs an occurrence-based approach (i.e., one AR "hit" for each 6 h period during which the criteria are met). As a result, the AR frequencies described herein are calculated based on the number of 6-hourly periods during which an AR exists over a given grid point or landfall boundary divided by the number of 6 h periods included in the composite. For example, Figure 1 shows the landfall boundaries overlaying the annual mean AR frequency of occurrence (ARF; shading) based on *Mundhenk et al.* [2016], updated to encompass the available 37 year MERRA record. Besides AR frequencies based on 6 h periods, ARs are also expressed in terms of unique events (i.e., one hit per feature life cycle), defined as the consecutive periods during which an AR is detected over a landfall boundary.

The boundaries approximating landfall shown in Figure 1 are each roughly 1200 km in length in order to facilitate the comparison of ARs near both locations. The number of AR periods is a function of the length of these landfall boundaries, increasing as the boundary length increases. The separation between the boundaries is deliberate in order to reduce the number of AR events that simultaneously impact both locations, while still representing regions of potential societal importance. Also, ARs need only graze a landfall boundary to be considered landfalling and included in these analyses. Though these boundaries are referred to as landfall boundaries, ARs are not restricted based on the angle of incidence. Although the nearly linear boundaries are oriented orthogonally, the results are similar if the boundaries are replaced with rectangular regions of equal area. In general, the results presented in this work are insensitive to small changes in the position and orientation of the landfall boundaries.

### 2.3. Atmospheric River Attributes

In addition to the location, date, and time of occurrence of each AR, the detection algorithm also quantifies specific attributes of each AR. Attributes assessed in this work include the following:

1. Persistence: approximate length of time, in hours, a unique AR event remains over a landfall boundary.
2. Length: approximate length, in kilometers, of an AR.
3. Area: approximate area, in square kilometers, of the region enclosed by an AR using the  $250 \text{ kg m}^{-1} \text{ s}^{-1}$  IVT' threshold.
4. Low-level zonal wind (u wind): mean of the layer averaged (1000–925 hPa) zonal wind within an AR.
5. Low-level meridional wind (v wind): mean of the layer averaged (1000–925 hPa) meridional wind within an AR.
6. Orientation: inclination of the mean low-level flow within an AR, in degrees, counterclockwise off the horizontal (e.g.,  $0^\circ$  is due east and  $90^\circ$  is due north).
7. Integrated water vapor transport (IVT): mean mass-weighted vertical integral of water vapor flux from 1000 to 300 hPa within an AR.
8. Integrated water vapor transport anomaly (IVT'): mean IVT, after the annual mean and seasonal cycle (calculated here as the first two harmonics of the annual climatology) have been removed via fast Fourier transform, within an AR.
9. Precipitable water (PWAT): mean mass-weighted vertical integral of tropospheric water vapor from 1000 to 300 hPa within an AR, also known as total precipitable water, total column water vapor, and/or integrated water vapor.

### 2.4. Rossby Wave Breaking Events

In order to associate AR events and height anomalies with Rossby wave breaking (RWB) activity in section 5, we draw upon the output of the Rossby wave identification algorithm of *Liu et al.* [2014]. This algorithm is based on *Strong and Magnusdottir* [2008] and is also used and further described in *Liu and Barnes* [2015]. *Liu et al.* [2014] interpolate 6-hourly MERRA potential temperature values ranging from 300 K to 350 K, at an interval of 5 K, onto the 2 potential vorticity unit (PVU) surface. If any of the potential temperature contours overturn and enclose an area of more than  $25^\circ$  on an equirectangular projection, an RWB event is identified and classified as either anticyclonic wave breaking (AWB) or cyclonic wave breaking (CWB) according to the direction of the overturning. Algorithm output is available for 1979–2010 at 6-hourly resolution. RWB climatologies based on this data set are available as Figures S1–S3 in the supporting information for reference.

For the results presented in section 5, the proximity of AR events to RWB activity is evaluated in both space and time. For each period during which a unique AR is detected over the respective boundary, the spatial extent of the AR is used to determine if the AR overlaps with a breaking region identified by the RWB detection scheme (that defined by the overturning potential temperature contours) during the same period. If an overlap is detected, the period is characterized by the amount of overlap and direction of the detected wave breaking. If no overlap is found, an additional check extends the AR extent by approximately  $3^\circ$  in all directions and repeats the test. The AR event is then classified based on the direction of the wave breaking occurring most often and with the greatest spatial overlap, giving preference to the overlap.

## 3. Occurrence and Attributes of Atmospheric Rivers

### 3.1. Atmospheric River Occurrences

We begin by assessing the existence of ARs over the landfall boundaries. Figure 3 reveals the presence of ARs within the 37 year reanalysis record over both boundaries as a function of overlapping 3 month seasons. ARs occur over both boundaries during each season; however, both locations display a pronounced seasonality in terms of the mean number of unique AR events (dotted curves; right ordinate), as well sizable interannual variability in the seasonal number of AR events (shading). The wintertime peak in AR activity along the U.S. West Coast is well documented [e.g., *Neiman et al.*, 2008b]. The shift in peak AR activity toward the Northern Hemisphere warm seasons at higher latitudes is also known [e.g., *Neiman et al.*, 2008a; *Mundhenk et al.*, 2016] and relates to the seasonal migration of the eddy-driven jet [*Mundhenk et al.*, 2016].

Figure 3 also depicts AR activity over the landfall boundaries in terms of frequency of occurrence (solid curves; left ordinate). Recall from section 2.2 that AR frequencies are based on the number of periods with an AR over a given landfall boundary divided by the total number of periods in each season, while the number of AR

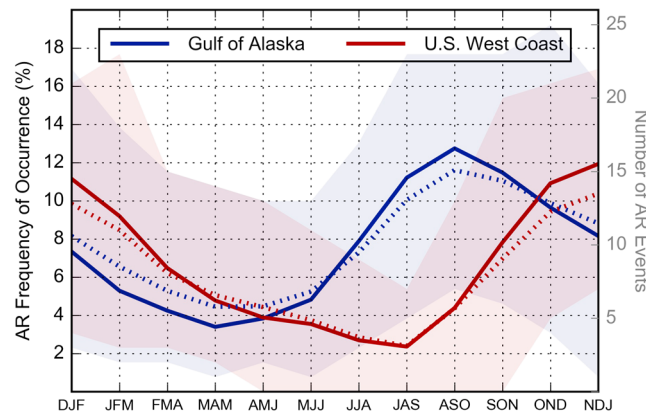


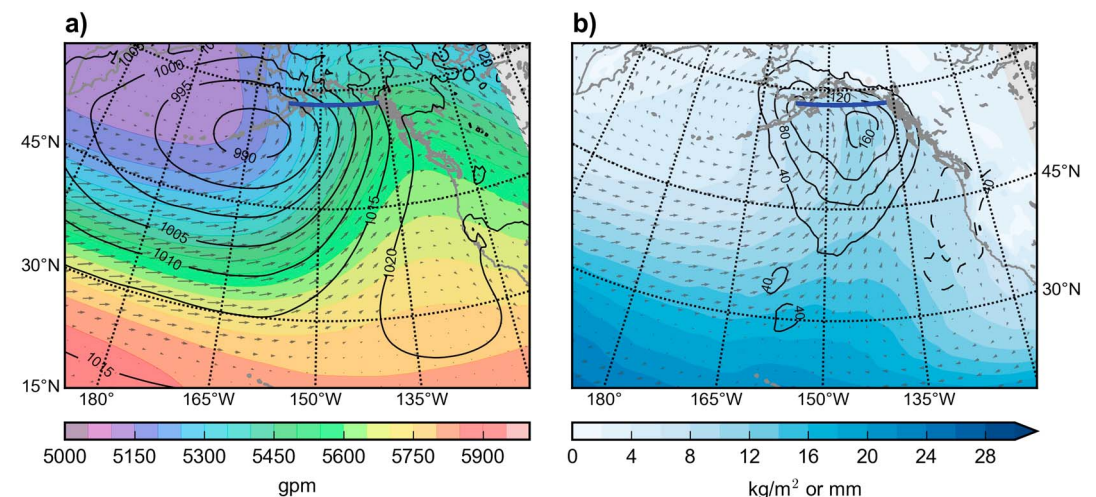
**Figure 3.** Seasonality of AR frequency of occurrence (solid curves; left ordinate) and the average number AR events (dotted curves; right ordinate) by overlapping 3 month seasons, each scaled to represent a uniform 90 day season, for the Gulf of Alaska (blue) and the U.S. West Coast (red) landfall boundaries. Shading highlights the range between the highest and lowest seasonal counts of AR events.

events consider the consecutive periods an AR exists over a boundary as one single event. The pronounced seasonality remains, with the AR frequencies peaking at nearly 12.7% for the Gulf of Alaska in August–October (ASO) and 11.9% for the U.S. West Coast in November–January (NDJ). Despite the difference in the AR seasonal cycle over the two landfall boundaries, the annual mean AR frequencies of 7.5% and 6.6%, for the Gulf of Alaska and U.S. West Coast, respectively, are comparable. As the seasonality of ARs along the west coast of North America is roughly a function of latitude, one may expect shifts in the curves in Figure 3 if the boundaries are adjusted meridionally.

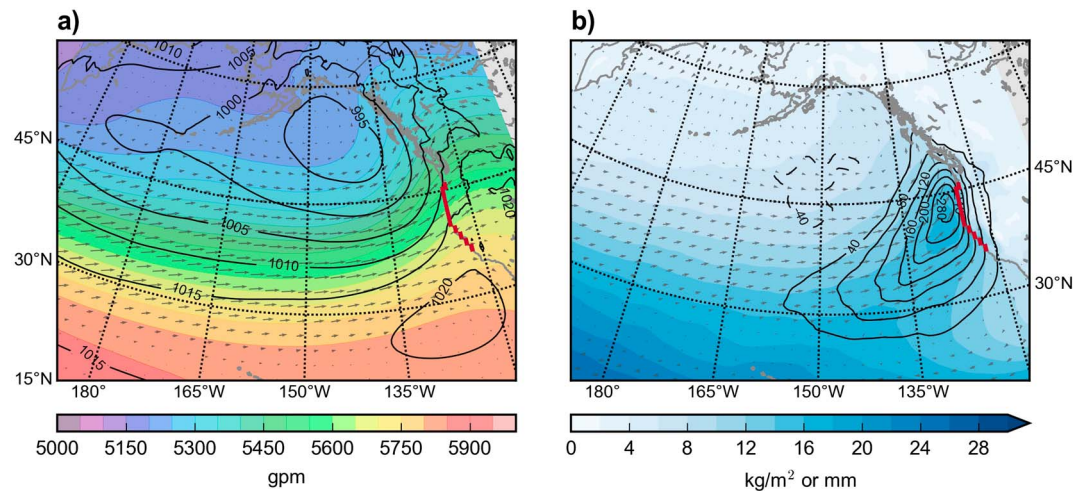
### 3.2. Composite Atmospheric Conditions

Figure 4 displays the composite atmospheric conditions for 383 unique AR events that passed over the Gulf of Alaska landfall boundary during December–February (DJF). DJF falls within the well-documented winter season for ARs along the U.S. West Coast and thus facilitates comparisons with findings from other studies. While the results throughout this section are discussed in terms of DJF and/or annual values, the majority of the relationships are not unique to a particular season and exist throughout the year.

The composite conditions in Figure 4 are based only on the first period from each AR event in order to best capture the conditions characteristic of initial landfall. Figure 4a shows a pronounced low-pressure system (contours) over the eastern Aleutian Islands. To the east, amplified 500 hPa ridging (shading) roughly aligns with the west coast of the North American continent (see Figure S4 in the supporting information for a comparison with the seasonal climatology). The resulting gradient between these features supports the abrupt transition from nearly zonal flow at 700 hPa over the central Pacific to meridional flow toward the landfall boundary (arrows). Figure 4b shows a tongue of high total precipitable water (shading) extending



**Figure 4.** Atmospheric conditions composited on the first period of the 383 unique DJF Gulf of Alaska AR events (blue demarcation). (a) Includes 500 hPa geopotential height (shading; intervals of 50 geopotential meters (gpm)), sea level pressure (black contours; intervals of 5 hPa), and 700 hPa vector winds (arrows). (b) The total precipitable water (shading; intervals of 2 mm), integrated water vapor transport anomalies (black contours; intervals of 40 kg m<sup>-1</sup> s<sup>-1</sup> with the zero contour omitted), and mean 1000–925 hPa winds (arrows).



**Figure 5.** As in Figure 4 but for composite first-period atmospheric conditions during 461 DJF U.S. West Coast AR events identified using the indicated landfall boundary (red demarcation).

toward southern Alaska coincident with strong low-level winds (arrows) and, therefore, a region of anomalous IVT (contours) encompassing the Gulf of Alaska landfall boundary. These characteristics are even more pronounced in composites where each AR's landfall position is shifted to a common longitude (not shown), confirming that the patterns in Figure 4 are smeared by variability along the 1200 km boundary. In their survey of subjectively selected rain and flooding events, *Papineau and Holloway* [2011] also found this general pattern of enhanced ridging over the far eastern Pacific and a broad, elongated low over the eastern Aleutians to be common among heavy rain events along the southern coast of Alaska.

Figure 5 depicts the atmospheric conditions composited from 461 first-period DJF U.S. West Coast AR events. A broad region of low pressure extends across the Gulf of Alaska and northeast Pacific in this composite. The pronounced 500 hPa ridging apparent in the Alaska composite (Figure 4a) is much weaker and farther inland in this U.S. West Coast AR analysis (Figure 5a). The flow at 700 hPa and at lower levels is predominantly zonal, with a subtle meridional perturbation just offshore of the west coast. Just as in the Gulf of Alaska AR composite, here a tongue of high total precipitable water extends from the semipersistent tropical moisture reservoir toward the landfall boundary (Figure 5b). The general composite conditions apparent in Figures 4 and 5 appear not only in these first-period composites but also in composites of conditions prior to landfall (not shown). This suggests that the tropospheric pattern that influences the location of AR landfall may begin to set up, in a composite sense, days prior to landfall.

### 3.3. Atmospheric River Attributes

Table 1 lists the mean attributes of ARs detected over the two landfall boundaries. Rather than using each AR event's first period as in Figures 4 and 5, Table 1 is constructed using mean attributes over the span of time each event persists over the landfall boundary. Boldface entries in Table 1 denote those attributes where the null hypothesis of equal means between the two locations can be rejected via a Welch's *t* test at the 95% confidence level.

Table 1 reveals that, on average, many attributes are similar for ARs near the two locations. More specifically, the annual mean AR persistence, length, area, IVT, IVT', and PWAT (see section 2.3 for definitions) are not statistically different. This suggests that the high-latitude ARs near Alaska are often comparable to their midlatitude counterparts. The mean AR attributes in Table 1 also afford comparisons with other AR studies. Indeed, it is shown here that the mean AR lengths exceed the well-accepted 2000 km length minimum threshold [e.g., *Ralph et al.*, 2004]. The mean values of PWAT equal the oft-used 2 cm (or 20 kg m<sup>-2</sup>) threshold in the annual mean analysis but fall just shy when assessed over DJF only. The 28 h mean persistence of annual U.S. West Coast ARs is longer than the 16 or 20 h (depending calculation method) mean persistence reported in *Ralph et al.* [2013], which was based on in situ observations of 91 ARs making landfall near California's Russian River basin. While this difference in mean persistence may be due to the larger domain used this study, it is more likely that this difference results from the 6-hourly reanalysis data used in this comparison versus the hourly observations used in *Ralph et al.* [2013].

**Table 1.** Mean AR Attributes<sup>a</sup>

Location	Events (Mean #)	Persistence (# Hours)	Length (km)	Orientation (deg)	Area (1000 km <sup>2</sup> )	<i>u</i> Wind (m s <sup>-1</sup> )	<i>v</i> Wind (m s <sup>-1</sup> )	IVT (kg m <sup>-1</sup> s <sup>-1</sup> )	IVT' (kg m <sup>-1</sup> s <sup>-1</sup> )	PWAT (kg m <sup>-2</sup> )
<i>Annual</i>										
Alaska	<b>40</b>	27	3383	<b>71</b>	1508	<b>2.1</b>	<b>11.9</b>	604	406	20
West Coast	<b>33</b>	28	3327	<b>58</b>	1532	<b>4.6</b>	<b>10.0</b>	599	406	20
<i>DJF</i>										
Alaska	<b>11</b>	<b>14</b>	<b>3591</b>	<b>84</b>	1563	<b>-0.9</b>	<b>15.4</b>	<b>577</b>	<b>401</b>	<b>17</b>
West Coast	<b>13</b>	<b>18</b>	<b>3190</b>	<b>49</b>	1637	<b>8.1</b>	<b>10.7</b>	<b>603</b>	<b>415</b>	<b>19</b>

<sup>a</sup>See section 2.3 for definitions of the attributes and acronyms. Boldface entries denote where the null hypothesis of equal means between the two locations can be rejected via Welch's *t* test at the 95% confidence level.

Some of the differences in the mean AR attributes in Table 1 can be visualized by the composite atmospheric conditions shown in Figures 4 and 5. For example, the abrupt shift from zonal to meridional flow over the North Pacific during DJF apparent in the composite of Gulf of Alaska ARs (Figure 4) substantiates the more north-south orientation, smaller mean low-level zonal winds (*u* wind), and greater mean low-level meridional winds (*v* wind) compared to the U.S. West Coast ARs. The difference between the mean AR lengths during DJF may be explained similarly. The Gulf of Alaska landfall boundary is farther removed from the mean position of the eddy-driven jet during the winter season; thus, ARs associated with eddies along the jet must be longer in length, on average, in order to reach the fixed high-latitude boundary. That relationship is lost in the annual comparison of AR lengths, likely due to the seasonal migration of the eddy-driven jet. Again, these results are insensitive to small changes in the position and orientation of the landfall boundaries.

### 3.4. Atmospheric Conditions Comparison

Figure 6 reveals the differences between the Gulf of Alaska DJF AR event composite (Figure 4a) and the U.S. West Coast DJF AR event composite (Figure 5a) for 500 hPa geopotential heights (shading), sea level pressure (contours), and 700 hPa winds (arrows). The dominant feature in this difference plot is the resulting

“anomalous” pressure, height, and circulation center in the northeast Pacific, for Gulf of Alaska ARs compared to U.S. West Coast ARs.

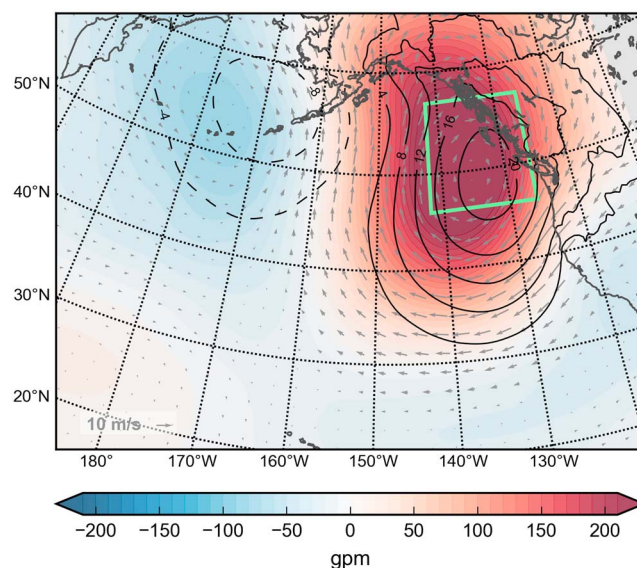


**Figure 6.** Differences between the DJF composite atmospheric conditions resulting from the subtraction of the U.S. West Coast event composite (Figure 5a) from the Gulf of Alaska event composite (Figure 4a) in 500 hPa geopotential height (shading), sea level pressure (black contours; intervals of 4 hPa with the zero contour omitted), and 700 hPa vector winds (arrows). The green box outlines the region in which height anomalies are assessed (see text for description).

The spatial pattern of the height difference in Figure 6 is not unique to DJF but is found in all seasons (not shown). The prevalence of this pattern motivates an assessment of the extent to which the anomaly feature over the northeast Pacific influences ARs near Alaska and the U.S. West Coast. Hereafter, this anomaly feature will be referred to as a geopotential height anomaly, but it may be thought of as a pressure or circulation anomaly too. To explore the relationship between this anomaly and ARs, we will evaluate 500 hPa geopotential height anomaly values (mean and seasonal cycle removed) averaged over the 11° × 16° region identified by the green box in Figure 6. The resulting time series has an *e*-folding decay time of approximately 12 days, suggesting that this anomaly is not just a transient feature associated with individual baroclinic waves. The height anomaly

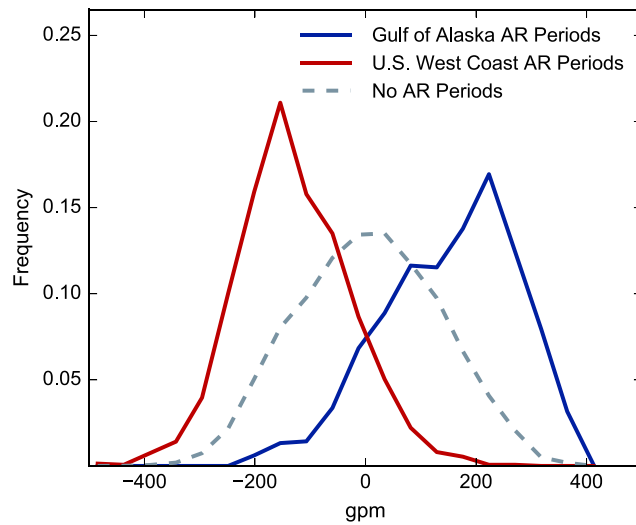


**Figure 7.** Distributions of mean 500 hPa geopotential height anomalies for the region identified in Figure 6 for all DJF periods during which an AR was detected along the Gulf of Alaska landfall boundary (blue), along the U.S. West Coast landfall boundary (red), and during which no AR was detected near either location (gray).

analysis box is located on the eastern periphery of the region of maximum annual geopotential height variability over the North Pacific (not shown). Shifting the box into the heart of the region of maximum variability may increase the dynamical signal but reduces the influence on AR activity along southern Alaska.

Figure 7 presents frequency distributions of DJF height anomaly values averaged over the region identified in Figure 6. Here each 6 h period is categorized based on whether an AR was detected over the Gulf of Alaska landfall boundary (blue), over the U.S. West Coast landfall boundary (red), or whether no AR was detected near either location (gray). Distinct distributions emerge. The distribution of height anomaly values associated with Gulf of Alaska AR periods is shifted toward

positive anomalies. In contrast, the distribution of height anomaly values associated with U.S. West Coast AR periods is shifted toward negative values. These opposing shifts agree with the difference plot (Figure 6) that depicts greater height anomaly values from the Gulf of Alaska DJF composite compared to the U.S. West Coast composite. Though the distributions in Figure 7 are based only on DJF, frequency distributions for other seasons are similar (not shown). Thus, we find that the composite results are not dominated by a few outlier events but rather represent the majority of ARs in the 37 year record.

Up to this point we have presented composites and distributions based on large samples of ARs. Here we briefly analyze two representative ARs, one detected over each of the landfall boundaries. Each of the two panels in Figure 8 displays an AR that generally exemplifies the DJF mean attributes (i.e., those in Table 1) for the respective boundary. The 500 hPa geopotential height anomalies (shading) and 700 hPa wind anomalies (arrows) in Figure 8a generally reflect the composite difference plot in Figure 6, with a pronounced positive height anomaly center in the northeast Pacific. We propound that the timing, location, and character of this anomaly is important to the existence of the AR extending from the central Pacific to the Gulf of Alaska

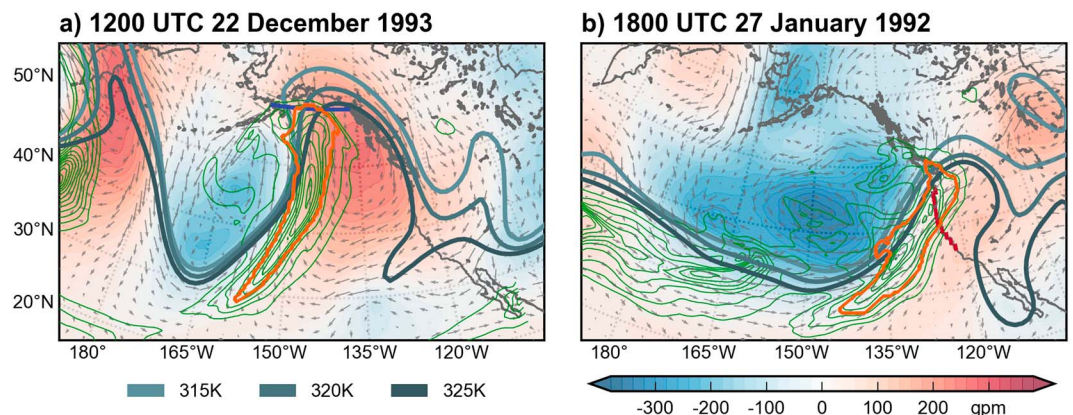


**Figure 8.** ARs (orange outlines) impacting the (a) Gulf of Alaska and (b) U.S. West Coast landfall boundaries. Each panel includes 500 hPa geopotential height anomalies (shading), 700 hPa vector wind anomalies (arrows), IVT (thin green contours; intervals of  $100 \text{ kg m}^{-1} \text{ s}^{-1}$  starting at  $200 \text{ kg m}^{-1} \text{ s}^{-1}$ ), and potential temperature contours on the 2 PVU surface used to assess Rossby wave breaking, smoothed via a 2 standard deviation multidimensional Gaussian filter (gray contours; 315–325 K). The potential temperature legend (left bottom) and color bar (right bottom) apply to both panels.

landfall boundary. The anomaly patterns in Figure 8b do not directly oppose those in Figure 8a, but a notable anomaly center of the opposite sign does extend into the northeast Pacific.

## 4. Atmospheric River Activity Across Time Scales

### 4.1. Synoptic Time Scale

From Figure 3 we appreciate that ARs are neither rare along the coast of southern Alaska nor the West Coast of the U.S. mainland. However, we find that ARs concurrently impacting both boundaries simultaneously are rather uncommon. That is, only approximately 3.9% of all Gulf of Alaska AR events temporally overlap an AR landfalling along the U.S. West Coast. Similarly, approximately 4.8% of the U.S. West Coast ARs overlap in time an AR near Alaska. This rarity of concurrent landfalling ARs suggests that a dynamical link may exist for these two landfall boundaries, such that AR activity near one boundary relates, in part, to opposing AR activity near the other boundary.

Together with Figure 7, the two ARs depicted in Figure 8 provide evidence that height anomalies in the northeast Pacific may influence individual ARs near both landfall boundaries and may be the dynamical link influencing AR activity. Here we extend the analysis of this relationship over the entire 37 year record to quantify the association between ARs and these height anomalies on the scale of unique AR events. Of the AR events detected over the Gulf of Alaska landfall boundary, approximately 79% are associated with a positive mean height anomaly over the analysis box identified in Figure 6. These percentages vary seasonally, for example, ranging from 72% in July–September (JAS) to 85% in February–April (FMA). The opposing relationship holds for the U.S. West Coast landfall boundary, where approximately 14% of the detected AR events are associated with a positive mean height anomaly, while 86% are associated with a negative anomaly. Thus, the ARs in Figure 8 are not outliers, but rather representative of a resilient relationship between northeast Pacific heights and AR activity on the scale of individual events.

The previous analysis assessed the northeast Pacific height anomaly and AR relationship in terms of individual AR events. If the relationship is robust and dynamically based, the relationship should also exist if assessed in terms of individual height anomaly events. Here height anomaly events are defined as consecutive 6 h periods during which the mean geopotential height anomaly within the analysis box maintains the same sign and meets or exceeds a  $\pm 1$  standard deviation ( $\sigma$ ) height anomaly threshold. When the 1 standard deviation threshold is used to define anomalous periods, the resulting height anomalies may hereafter be denoted as  $H'$ .

The probability of any AR occurring over the Gulf of Alaska boundary during a strong  $+H'$  event is approximately 49% (see Table 2). That is to say, 49% of the 907  $+H'$  events within the 37 year record contain at least one period of time when an AR is detected near Alaska. In contrast, the probability of a Gulf of Alaska AR during a  $-H'$  event drops to 6%. For the U.S. West Coast, the probability of an AR occurring is 3% and 45% during a  $+H'$  event and a  $-H'$  event, respectively. As with other measures, these probabilities vary seasonally but generally follow the seasonality of ARs exhibited in Figure 3. These numbers indicate that the probability of any AR occurring may change drastically based on the state of the atmosphere over the northeast Pacific. While these calculations are based on  $\pm 1$  standard deviation thresholds, we find that a threshold of zero shows the same, yet weaker, relationships (not shown), and still indicates that the probability of any AR occurring may double or even triple based on tropospheric height conditions in the northeast Pacific.

The probabilities in Table 2 are, perhaps, more meaningful when compared to rates of AR occurrence approximated by 10,000 bootstrap iterations. Each bootstrap iteration is constructed using the same number and duration of  $H'$  events as exist in the MERRA-based time series, with the starting periods randomly selected from the 37 year record. As constructed, this bootstrap analysis provides estimates of the probability of any AR occurring over the boundaries if no dynamical relationship with northeast Pacific height anomalies exists. For both landfall boundaries, we find that the actual AR probabilities exceed the 95% confidence bounds of the bootstrap distribution (given in Table 2), thus providing strong evidence of a dynamical link between  $H'$  and AR activity on the synoptic time scale.

The consistency of the northeast Pacific height anomaly and AR activity relationship regardless of whether it is evaluated based on AR events or height anomaly events demonstrates the robustness of the relationship. These analyses imply that this mechanistic relationship may provide predictability, such that knowledge of the current or future state of the large-scale flow over the northeast Pacific may provide information about the likelihood of AR activity. For example, if a broad, positive height anomaly is expected to build over the

**Table 2.** Percent of  $H'$  Events With  $\geq 1$  AR Period<sup>a</sup>

Location	+ $H'$	- $H'$
Gulf of Alaska	<b>49%</b> (21–26%)	<b>6%</b> (19–24%)
U.S. West Coast	<b>3%</b> (17–22%)	<b>45%</b> (15–20%)

<sup>a</sup>Values in the parentheses represent the 95% confidence bounds from the distribution of 10,000 bootstrap iterations. Boldface entries denote where the actual AR probability exceeds the 95% confidence bounds of the bootstrap distribution.

northeast Pacific and persist for approximately 1 week, the likelihood of AR activity near the Gulf of Alaska landfall boundary will be higher than climatology as a result, and the likelihood of AR activity near the U.S. West Coast will be lower than climatology, so long as the height anomaly persists.

Ralph *et al.* [2013] documented that an AR's persistence over an area strongly influences its potential postlandfall impacts (e.g., heavy rainfall and flash flooding). Here we assess the combined influence of the total number, spatial extent, and persistence of ARs by considering AR frequencies (ARF). The seasonally varying ARF for the two landfall boundaries are shown in Figure 3 and repeated as the dotted curves in Figure 9. Atmospheric river frequencies parsed by positive and negative height anomalies meeting or exceeding the respective 1 standard deviation threshold are also plotted (solid and dashed curves, respectively) for both landfall boundaries. Though the curves in Figure 9 display a pronounced seasonality, the percent increase or decrease relative to the seasonally varying ARF are nearly constant throughout the year. Strong positive northeast Pacific height anomalies increase the ARF for the Gulf of Alaska boundary to nearly 22%, as compared to the annual mean frequency of 7.5%. The same positive height anomalies decrease the ARF for the U.S. West Coast boundary to less than 1%, or less than one tenth of the annual mean frequency of 6.6%. Strong negative height anomalies have the opposite impact over the two locations of interest, decreasing the Gulf of Alaska ARF to 1% and increasing the U.S. West Coast ARF to 24%.

#### 4.2. Subseasonal Time Scale

Finding a robust relationship between broad northeast Pacific height anomalies and AR activity at the synoptic time scale, we now assess whether the relationship holds for longer time scales. Extending the analysis to the subseasonal time scale, we consider the 444 calendar months in the 37 year record. A month is categorized as positive or negative  $H'$  if the month's mean anomaly value meets or exceeds a respective 1 standard deviation threshold. Similarly, a month is characterized as having increased or decreased AR activity based on the total number of AR periods in the month compared to climatology. The monthly values are compared to monthly climatologies; thus, variability beyond subseasonal time scales (interannual, decadal, etc.) are retained in this analysis.

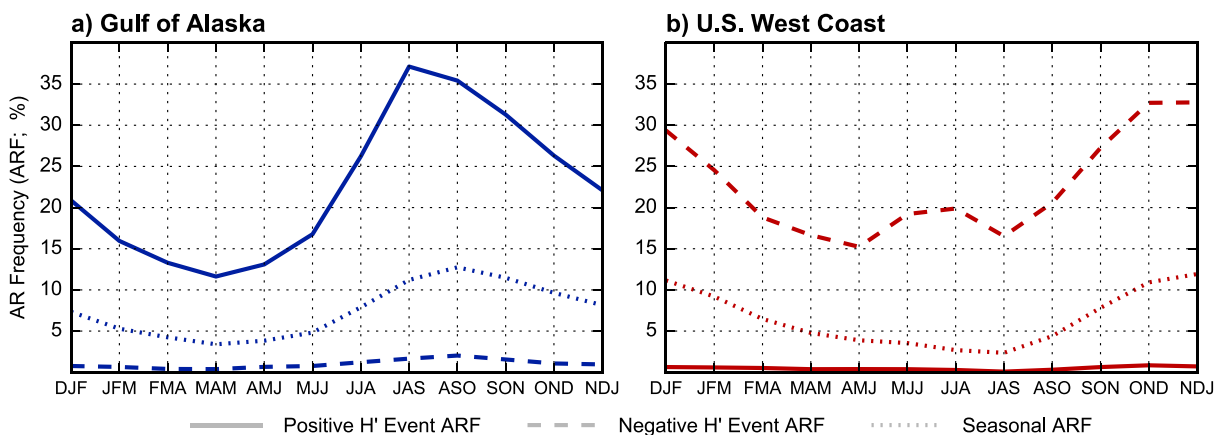


**Figure 9.** Seasonality of the impact of northeast Pacific 500 hPa geopotential height anomalies ( $H'$ ) meeting or exceeding a  $1\sigma$  threshold on AR frequency of occurrence (ARF) for the (a) Gulf of Alaska and (b) U.S. West Coast landfall boundaries. The solid curves represent the ARF during positive height anomaly events, the dashed curves represent the ARF during negative height anomaly events, and the dotted curves show the seasonal ARF (as shown in Figure 3) for comparison.

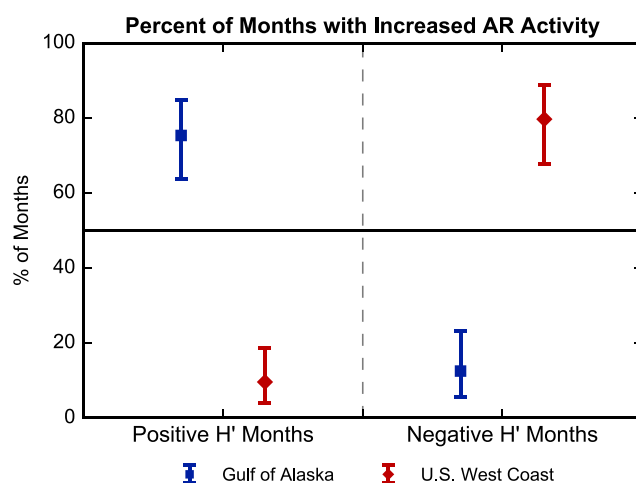


**Figure 10.** Comparison of the percent of months with increased AR activity during months with (left column) mean positive northeast Pacific 500 hPa geopotential height anomalies  $\geq 1\sigma$  and (right column) mean negative height anomalies  $\leq -1\sigma$  for the Gulf of Alaska (blue with square markers) and U.S. West Coast (red with diamond markers). Error bars encompass the 95% confidence interval for a binomial distribution based on the Clopper-Pearson method [Clopper and Pearson, 1934].

Figure 10 depicts the percent of calendar months with increased AR activity at each landfall boundary based on the monthly height anomaly. We find opposing AR activity during months with positive and negative height anomalies for the two landfall boundaries. For example, nearly 75% of the months with mean positive height anomalies meeting or exceeding 1 standard deviation have increased AR activity over the Gulf of Alaska, compared to only 13% with a mean negative height anomaly. For the U.S. West Coast, less than 10% of positive height anomaly months have increased AR activity, compared to nearly 80% of negative height anomaly months. The separation between the error bars, representing the 95% confidence intervals, for each location suggests a significant relationship at subseasonal resolution.

The results depicted in Figure 10 consider the height anomaly and AR activity relationship separately for each of the landfall boundaries. Here we expand the analysis to assess the combined, opposing response of AR activity at both locations (i.e., an increase in AR activity near Alaska together with a decrease in U.S. West Coast AR activity coincident with a positive height anomaly). We find that 69% of the months meeting or exceeding the 1 standard deviation height anomaly threshold exhibit a combined response in accordance with the northeast Pacific height anomaly and AR mechanistic relationship for both boundaries. Only 2% of the months display combined AR activity counter to the postulated relationships (i.e., a decrease in Alaska AR activity together with an increase in U.S. West Coast AR activity coincident with a positive height anomaly). However, 29% of the months show the same sign of anomalous AR activity over both boundaries regardless of the height anomaly, suggesting that a northeast Pacific height anomaly is not the sole mechanism responsible for subseasonal AR variability over the two landfall boundaries explored here.

### 4.3. Interannual Time Scale

We further extend our analysis to interannual anomalies, briefly evaluating year-to-year variations in the 36 extended boreal winter seasons (November–March (NDJFM)) within the MERRA reanalysis data set. Here we explore whether seasons with notable mean height anomalies in the northeast Pacific, such as the persistent anomalous ridging that occurred during the winter of 2013–2014 [e.g., Wang *et al.*, 2014; Lee *et al.*, 2015; Bond *et al.*, 2015], also have anomalous AR activity over the landfall boundaries. AR activity in the Gulf of Alaska is increased during only 52% of winter seasons with a mean positive northeast Pacific height anomaly and decreased during 60% of the seasons with a mean negative height anomaly. AR activity near the U.S. West Coast, however, exhibits the expected decrease in AR activity during 71% of seasons with a mean positive height anomaly and increase during 73% of the seasons with a mean negative anomaly. The higher percentages for the U.S. West Coast boundary suggest that the height anomaly box used in this study is positioned to better represent the forcing for interannual variability in wintertime AR activity for the U.S. West Coast than for Alaska.

These initial winter seasonal statistics are based solely on the signs of the mean NDJFM height anomalies. Next we assess the interannual relationship between anomalous heights and AR activity and also include information regarding the strength of the height anomalies. Figure 11 reveals the relationship between the total number of AR periods over each landfall boundary during each winter season compared to the mean height anomaly values. For the U.S. West Coast (red), we find an inverse relationship between AR activity and the height anomaly strength. A linear best fit line accounts for approximately 44% of the total variance. The opposite relationship exists for the Gulf of Alaska boundary (blue), where AR activity increases together

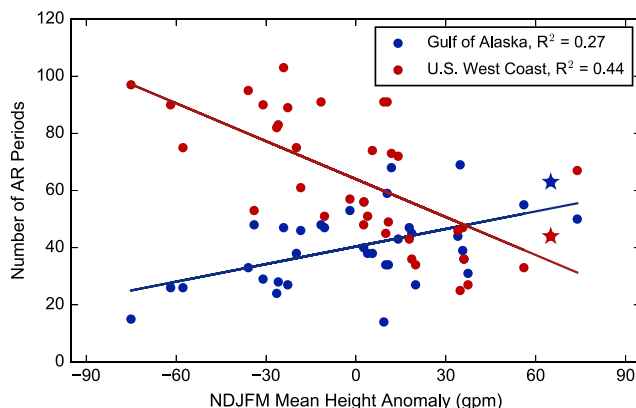


**Figure 11.** Relationship between the total number of extended boreal winter (NDJFM) AR periods and the mean northeast Pacific height anomaly value, for the Gulf of Alaska (blue) and U.S. West Coast (red) landfall boundaries. Each winter season is indicated by a colored circle for each boundary, while the 2013–2014 season noted in the text is identified by the stars. Solid lines represent the linear best fit, with the respective  $R^2$  values listed in the legend.

with the strength of the mean height anomaly; the associated linear best fit line accounts for 27% of the variance. Thus, the relationship between height anomalies and AR activity identified at shorter time scales holds in terms of interannual variability.

Based on this analysis, the anomalous ridging that persisted over the northeast Pacific for much of the winter of 2013–2014 [see, e.g., Hartmann, 2015, Figure 3a] was the second strongest of the 36 winter seasons (stars in Figure 11). AR activity was also extremely high over the Gulf of Alaska (third highest total number of AR periods out of the 36 seasons) and low over the U.S. West Coast (eighth lowest of the 36 seasons) during the winter of 2013–2014. See Table S1 in

the supporting information for a full listing of winter season ranks and values. This analysis suggests that the inclusion of a measure of the magnitude of height anomalies bolsters the mechanistic relationship between northeast Pacific height anomalies and AR activity at the interannual time scale.

### 5. Links to Large-Scale Dynamics

The preceding section documents a robust relationship between ARs both near southern Alaska and the U.S. West Coast and height anomalies over the northeast Pacific. The results suggest that this relationship applies across a range of time scales, from that of individual ARs and height anomaly events to interannual time scales. In an effort to link this relationship to the large-scale dynamics over the North Pacific, we are inspired by the documented association between wintertime ARs along the U.S. West Coast and Rossby wave breaking (RWB) [e.g., Ryoo et al., 2013; Payne and Magnusdottir, 2014].

Using the RWB event atlas described in section 2.4, unique AR events may be linked in time and space with nearby RWB activity. For example, the representative ARs in Figure 8 are found to be associated with a developing cyclonic wave breaking (CWB) event and an anticyclonic wave breaking (AWB) event, for Figures 8a and

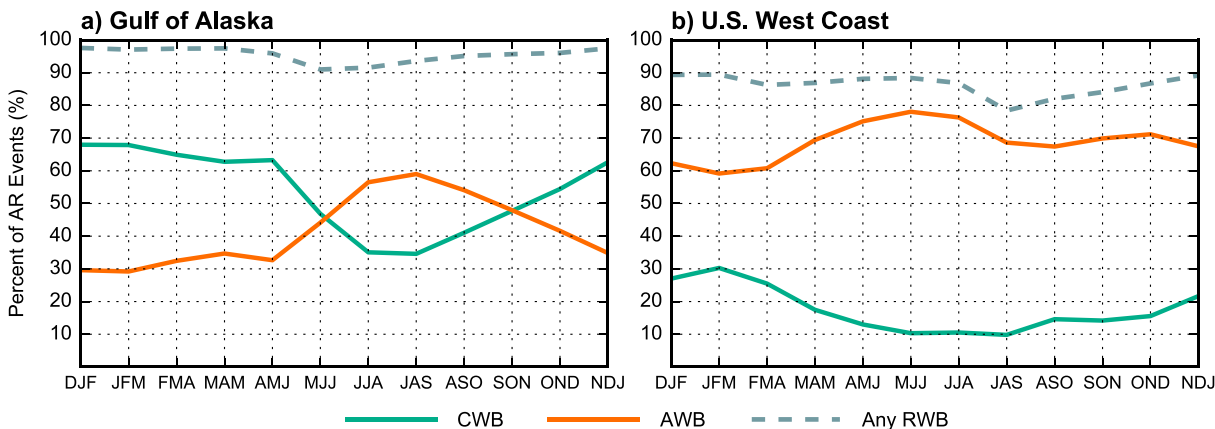


**Figure 12.** Seasonality of the percent of AR events from 1979 to 2010 associated with Rossby wave breaking for the (a) Gulf of Alaska and (b) U.S. West Coast landfall boundaries. The colors denote different wave breaking directions with green representing cyclonic wave breaking (CWB) and orange representing anticyclonic wave breaking (AWB). The dashed gray curve in each panel represents the percent of AR events associated with any breaking event, regardless of type.

8b, respectively (see the gray contours). Figure 12 reveals the percent of all AR events associated with CWB (green) and AWB (orange) for each of the landfall boundaries in terms of overlapping 3 month seasons.

Over the Gulf of Alaska, ARs are collocated with both types of wave breaking throughout the year, as shown in Figure 12a. The seasonality in the dominant wave breaking direction may be attributed to the seasonal migration of the eddy-driven jet over the North Pacific. The Gulf of Alaska landfall boundary is positioned well poleward of the climatological jet position in boreal winter, thus in a region of cyclonic shear and favored CWB from OND to AMJ. As the jet migrates poleward during boreal spring and then retreats in the autumn, the landfall boundary is nearer the jet core itself, thus subject to cyclonic and/or anticyclonic shear, and associated wave breaking, as perturbations propagate through. During a brief period during boreal summer (JJA–ASO), AWB dominates. Over the period 1979–2010, approximately 95% of all of the AR events detected over the Gulf of Alaska boundary are associated with RWB (dashed gray curve).

Figure 12b shows the percent of U.S. West Coast AR events associated with wave breaking, parsed by wave breaking direction. The U.S. West Coast boundary exhibits far less seasonal variability than the Gulf of Alaska boundary, and the apparent year-round link between ARs and AWB can be explained by the prevalence of anticyclonic breaking equatorward of the mean jet position [e.g., Payne and Magnusdottir, 2014]. Overall, nearly 86% of all AR events over the U.S. West Coast are associated with RWB.

Similarly, northeast Pacific height anomaly events are associated with nearby RWB activity. Over the northeast Pacific anomaly analysis box, the onset of approximately 97% of the positive height anomaly events that persist for at least 2 days during 1979–2010 spatially and temporally coincide with RWB. Here height anomaly events are defined as those meeting or exceeding a 1 standard deviation anomaly threshold and the onset defined as the 24 h leading up to and including the first period when that is met. The 97% value exceeds the 99.9th percentile of a distribution of 10,000 bootstrap simulations of RWB occurrence with randomly selected onset periods. As defined, these broad, persistent positive height anomalies may be thought of as blocking anticyclones, the onset of which are often associated with the breaking of upper level Rossby waves [e.g., Pelly and Hoskins, 2003; Berrisford et al., 2007; Woolings et al., 2008; Tyrlis and Hoskins, 2008]. As a result, RWB should be considered integral to what we refer to in this work as positive northeast Pacific height anomalies.

Landfalling ARs and northeast Pacific height anomalies are both associated with Rossby wave breaking. Consequently, the mechanistic relationship identified in this work that relates AR activity near the landfall boundaries with northeast Pacific height anomalies is linked to the dynamics of the broader North Pacific. This dynamical linkage may bolster the understanding of periods of anomalous AR activity. For example, the documented relationships between organized tropical convection and remote Rossby wave activity [e.g., Moore et al., 2010; Adames and Wallace, 2014; Branstator, 2014] may help explain variability in AR activity over the west coast of North America, though a more extensive analysis shall remain for future work.

## 6. Conclusions

ARs occur throughout the year near southern Alaska and the U.S. West Coast. Climatologically, AR activity over both boundaries displays a pronounced seasonal cycle, peaking in August–October (ASO) near Alaska and in November–January (NDJ) near the U.S. West Coast. We find that, on average, AR attributes such as their persistence, length, area, IVT, IVT', and PWAT are comparable for ARs in both regions, while attributes such as their orientation and low-level wind speeds often differ.

A comparison of composite atmospheric conditions over the North Pacific during Gulf of Alaska and U.S. West Coast AR events reveals a broad anomaly over the northeast Pacific differentiating the contrasting composites. Though this anomaly feature may be characterized as a pressure and/or circulation anomaly, we define it in terms of a 500 hPa geopotential height anomaly. Quantitatively, nearly 79% of Gulf of Alaska ARs are associated with a positive northeast Pacific height anomaly and 86% of U.S. West Coast ARs are associated with a negative anomaly. Therefore, the composites used in the comparison are not dominated by a few outlier events, but rather representative of the majority of ARs detected near the landfall boundaries.

We find that these height anomalies over the northeast Pacific are influential to AR activity over both landfall boundaries, presenting an AR activity “trade-off” between the two locations. When a positive height anomaly exists over the northeast Pacific, AR activity is often deflected poleward toward Alaska. This increase in AR activity near Alaska comes at the cost of AR activity along the U.S. West Coast, which experiences a decrease in AR activity relative to climatology. The opposing relationship also applies; that is, AR activity is decreased

near Alaska and increased along the west coast of the U.S. in the presence of a negative northeast Pacific height anomaly.

Results indicate that this modulation of AR activity is robust, as the impacts on AR activity are consistent and quantifiable in terms of AR events, height anomaly events, and AR frequencies. We find that the anomalous circulation associated with broad northeast Pacific height anomalies influences the landfall location and character of ARs. However, height anomalies in the northeast Pacific analysis box alone are insufficient to account for all of the variability in AR activity (see the distribution spread in Figure 7).

The modulation of AR activity by northeast Pacific height anomalies applies not only at the synoptic time scale but also at subseasonal and interannual time scales. For example, we find that the anomalous ridging that persisted over the northeast Pacific for much of the winter of 2013–2014 coincided with anomalously high AR activity near the Gulf of Alaska boundary and low AR activity near the U.S. West Coast boundary over the same period.

Landfalling ARs and persistent positive northeast Pacific height anomalies are both found to be associated with Rossby wave breaking, thereby dynamically linking AR activity and blocking-like height anomalies with broader North Pacific dynamics. These dynamical relationships may be exploited to assess, and perhaps predict, anomalous AR activity. For example, *Henderson et al.* [2016] found a near doubling of the frequency of wintertime East Pacific blocking events following the propagation of the intraseasonal Madden-Julian oscillation's (MJO's) active phase over the western Pacific (i.e., the real-time multivariate MJO index's phase 7). After compositing AR occurrences by the state of the MJO, both *Guan and Waliser* [2015] and *Mundhenk et al.* [2016] found increased AR frequencies over portions of the northeast Pacific associated with similar MJO phase events.

Together with the investigation of AR occurrences and their composite atmospheric conditions, the Rossby wave breaking evaluation and related dynamical analysis afford a better understanding of the dynamics supporting high-latitude ARs over the North Pacific compared to their midlatitude counterparts. Though the predictive skill of the mechanistic relationship is not quantified in this study, knowledge of the current or future state of the large-scale flow over the northeast Pacific may provide valuable, predictive information about the likelihood of AR activity over a range of time scales.

#### Acknowledgments

The authors thank Chengji Liu for providing his Rossby wave breaking data and NASA's Global Modeling and Assimilation Office and Goddard Earth Sciences Data and Information Services Center (<http://disc.sci.gsfc.nasa.gov/>) for the MERRA reanalysis data. Thanks also to the Editor and three anonymous reviewers whose constructive comments materially improved this manuscript. This study was supported, in part, by the National Science Foundation's Climate and Large-Scale Dynamics Program under grants AGS-1419818 and AGS-1441916 and Educational Linkages Program under grant AGS-1461270.

#### References

- Adames, Á. F., and J. M. Wallace (2014), Three-dimensional structure and evolution of the MJO and its relation to the mean flow, *J. Atmos. Sci.*, *71*, 2007–2026, doi:10.1175/JAS-D-13-0254.1.
- Berrisford, P., B. J. Hoskins, and E. Tyrlis (2007), Blocking and Rossby wave breaking on the dynamical tropopause in the Southern Hemisphere, *J. Atmos. Sci.*, *64*, 2881–2898, doi:10.1175/JAS3984.1.
- Bond, N. A., M. F. Cronin, H. Freeland, and N. Mantua (2015), Causes and impacts of the 2014 warm anomaly in the NE Pacific, *Geophys. Res. Lett.*, *42*, 3414–3420, doi:10.1002/2015GL063306.
- Brands, S., J. M. Gutiérrez, and D. San-Martín (2016), Twentieth-century atmospheric river activity along the west coasts of Europe and North America: Algorithm formulation, reanalysis uncertainty and links to atmospheric circulation patterns, *Clim. Dyn.*, *1–25*, doi:10.1007/s00382-016-3095-6.
- Branstator, G. (2014), Long-lived response of the midlatitude circulation and storm tracks to pulses of tropical heating, *J. Clim.*, *27*, 8809–8826, doi:10.1175/JCLI-D-14-00312.1.
- Clopper, C., and E. S. Pearson (1934), The use of confidence or fiducial limits illustrated in the case of the binomial, *Biometrika*, *26*, 404–413, doi:10.1093/biomet/26.4.404.
- Dettinger, M. D. (2013), Atmospheric rivers as drought busters on the U.S. West Coast, *J. Hydrometeorol.*, *14*, 1721–1732, doi:10.1175/JHM-D-13-02.1.
- Dettinger, M. D., F. M. Ralph, T. Das, P. J. Neiman, and D. R. Cayan (2011), Atmospheric rivers, floods, and the water resources of California, *Water*, *3*, 445–478, doi:10.3390/w3020445.
- Dufour, A., O. Zolina, and S. K. Gulev (2016), Atmospheric moisture transport to the Arctic: Assessment of reanalyses and analysis of transport components, *J. Clim.*, *29*, 5061–5081, doi:10.1175/JCLI-D-15-0559.1.
- Guan, B., and D. E. Waliser (2015), Detection of atmospheric rivers: Evaluation and application of an algorithm for global studies, *J. Geophys. Res. Atmos.*, *120*, 12,514–12,535, doi:10.1002/2015JD024257.
- Guan, B., N. P. Molotch, D. E. Waliser, E. J. Fetzer, and P. J. Neiman (2012), Extreme snowfall events linked to atmospheric rivers and surface air temperature via satellite measurements, *Geophys. Res. Lett.*, *37*, L20401, doi:10.1029/2010GL044696.
- Hartmann, D. L. (2015), Pacific sea surface temperature and the winter of 2014, *Geophys. Res. Lett.*, *42*, 1894–1902, doi:10.1002/2015GL063083.
- Henderson, S. A., E. D. Maloney, and E. A. Barnes (2016), The influence of the Madden–Julian oscillation on Northern Hemisphere winter blocking, *J. Clim.*, *29*, 4597–4616, doi:10.1175/JCLI-D-15-0502.1.
- Jackson, D. L., M. Hughes, and G. A. Wick (2016), Evaluation of landfalling atmospheric rivers along the U.S. West Coast in reanalysis data sets, *J. Geophys. Res. Atmos.*, *121*, 2705–2718, doi:10.1002/2015JD024412.
- Lee, M.-Y., C.-C. Hong, and H.-H. Hsu (2015), Compounding effects of warm sea surface temperature and reduced sea ice on the extreme circulation over the extratropical North Pacific and North America during the 2013–2014 boreal winter, *Geophys. Res. Lett.*, *42*, 1612–1618, doi:10.1002/2014GL062956.

- Liu, C., and E. A. Barnes (2015), Extreme moisture transport into the Arctic linked to Rossby wave breaking, *J. Geophys. Res. Atmos.*, *120*, 3774–3788, doi:10.1002/2014JD022796.
- Liu, C., X. Ren, and X. Yang (2014), Mean flow-storm track relationship and Rossby wave breaking in two types of El-Niño, *Adv. Atmos. Sci.*, *31*, 197–210, doi:10.1007/s00376-013-2297-7.
- Moore, R. W., O. Martius, and T. Spengler (2010), The modulation of the subtropical and extratropical atmosphere in the Pacific basin in response to the Madden-Julian oscillation, *Mon. Weather Rev.*, *138*, 2761–2779, doi:10.1175/2010MWR3194.1.
- Mundhenk, B. D., E. A. Barnes, and E. D. Maloney (2016), All-season climatology and variability of atmospheric river frequencies over the North Pacific, *J. Clim.*, *29*, 4885–4903, doi:10.1175/JCLI-D-15-0655.1.
- Neiman, P. J., F. M. Ralph, G. A. Wick, J. D. Lundquist, and M. D. Dettinger (2008a), Meteorological characteristics and overland precipitation impacts of atmospheric rivers affecting the west coast of North America based on eight years of SSM/I satellite observations, *J. Hydrometeorol.*, *9*, 22–47, doi:10.1175/2007JHM855.1.
- Neiman, P. J., F. M. Ralph, G. A. Wick, Y.-H. Kuo, T.-K. Wee, Z. Ma, G. H. Taylor, and M. D. Dettinger (2008b), Diagnosis of an intense atmospheric river impacting the Pacific Northwest: Storm summary and offshore vertical structure observed with COSMIC satellite retrievals, *Mon. Weather Rev.*, *138*, 4398–4420, doi:10.1175/2008MWR2550.1.
- Neiman, P. J., L. J. Schick, F. M. Ralph, M. Hughes, and G. A. Wick (2011), Flooding in western Washington: The connection to atmospheric rivers, *J. Hydrometeorol.*, *12*, 1337–1358, doi:10.1175/2011JHM1358.1.
- Papineau, J., and E. Holloway (2011), The nature of heavy rain and flood events in Alaska, Anchorage Forecast Office Research Papers, NOAA/NWS/ARH. [Available online at <http://citeseerx.ist.psu.edu/viewdoc/summary?doi=10.1.1.729.6444>.]
- Papineau, J., and E. Holloway (2012), The dry side of atmospheric rivers in Alaska, Anchorage Forecast Office Research Papers, NOAA/NWS/ARH. [Available online at <http://citeseerx.ist.psu.edu/viewdoc/summary?doi=10.1.1.729.4947>.]
- Payne, A. E., and G. Magnusdottir (2014), Dynamics of landfalling atmospheric rivers over the North Pacific in 30 years of MERRA reanalysis, *J. Clim.*, *27*, 7133–7150, doi:10.1175/JCLI-D-14-00034.1.
- Pelly, J. L., and B. J. Hoskins (2003), A new perspective on blocking, *J. Atmos. Sci.*, *60*, 743–755, doi:10.1175/1520-0469(2003)060<0743:ANPOB>2.0.CO;2.
- Radić, V., A. J. Cannon, B. Menounos, and N. Gi (2015), Future changes in autumn atmospheric river events in British Columbia, Canada, as projected by CMIP5 global climate models, *J. Geophys. Res. Atmos.*, *120*, 9279–9302, doi:10.1002/2015JD023279.
- Ralph, F. M., and M. D. Dettinger (2012), Historical and national perspectives on extreme West Coast precipitation associated with atmospheric rivers during December 2010, *Bull. Am. Meteorol. Soc.*, *93*, 783–790, doi:10.1175/BAMS-D-11-00188.1.
- Ralph, F. M., P. J. Neiman, and G. A. Wick (2004), Satellite and CALJET aircraft observations of atmospheric rivers over the eastern North Pacific ocean during the winter of 1997/98, *Mon. Weather Rev.*, *132*, 1721–1745, doi:10.1175/1520-0493(2004)132<1721:SACAOO>2.0.CO;2.
- Ralph, F. M., P. J. Neiman, G. A. Wick, S. I. Gutman, M. D. Dettinger, D. R. Cayan, and A. B. White (2006), Flooding on California's Russian River: The role of atmospheric rivers, *Geophys. Res. Lett.*, *33*, L13801, doi:10.1029/2006GL026689.
- Ralph, F. M., T. Coleman, P. J. Neiman, R. J. Zamora, and M. D. Dettinger (2013), Observed impacts of duration and seasonality of atmospheric-river landfalls on soil moisture and runoff in coastal Northern California, *J. Hydrometeorol.*, *14*, 443–459, doi:10.1175/JHM-D-12-076.1.
- Rienecker, M. M., et al. (2011), MERRA: NASA's Modern-Era Retrospective Analysis for Research and Applications, *J. Clim.*, *24*, 3624–3648, doi:10.1175/JCLI-D-11-00015.1.
- Roberge, A., J. R. Gyakum, and E. H. Atallah (2009), Analysis of intense poleward water vapor transports into high latitudes of western North America, *Weather Forecasting*, *24*, 1732–1747, doi:10.1175/2009WAF222198.1.
- Rutz, J. J., W. J. Steenburgh, and F. M. Ralph (2014), Climatological characteristics of atmospheric rivers and their inland penetration over the western United States, *Mon. Weather Rev.*, *142*, 905–920, doi:10.1175/MWR-D-13-00168.1.
- Ryoo, J.-M., Y. Kaspi, D. W. Waugh, G. N. Kiladis, D. E. Waliser, E. J. Fetzer, and J. Kim (2013), Impact of Rossby wave breaking on U.S. West Coast winter precipitation during ENSO events, *J. Clim.*, *26*, 6360–6382, doi:10.1175/JCLI-D-12-00297.1.
- Smith, B. L., S. E. Yuter, P. J. Neiman, and D. E. Kingsmill (2010), Water vapor fluxes and orographic precipitation over Northern California associated with a landfalling atmospheric river, *Mon. Weather Rev.*, *138*, 74–100, doi:10.1175/2009MWR2939.1.
- Strong, C., and G. Magnusdottir (2008), Tropospheric Rossby wave breaking and the NAO/NAM, *J. Atmos. Sci.*, *65*, 2861–2876, doi:10.1175/2008JAS2632.1.
- Tyrlis, E., and B. J. Hoskins (2008), The morphology of Northern Hemisphere blocking, *J. Atmos. Sci.*, *65*, 1653–1665, doi:10.1175/2007JAS2338.1.
- Wang, S.-Y., L. Hippos, R. R. Gillies, and J.-H. Yoon (2014), Probable causes of the abnormal ridge accompanying the 2013–2014 California drought: ENSO precursor and anthropogenic warming footprint, *Geophys. Res. Lett.*, *41*, 3220–3226, doi:10.1002/2014GL059748.
- Warner, M. D., C. F. Mass, and E. P. Salathé Jr. (2012), Wintertime extreme precipitation events along the Pacific Northwest coast: Climatology and synoptic evolution, *Mon. Weather Rev.*, *140*, 2021–2043, doi:10.1175/MWR-D-11-00197.1.
- Woods, C., and R. Caballero (2016), The role of moist intrusions in winter Arctic warming and sea ice decline, *J. Clim.*, *29*, 4473–4485, doi:10.1175/JCLI-D-15-0773.1.
- Woods, C., R. Caballero, and G. Svensson (2013), Large-scale circulation associated with moisture intrusions into the Arctic during winter, *Geophys. Res. Lett.*, *40*, 4717–4721, doi:10.1002/grl.50912.
- Woolings, T., B. Hoskins, M. Blackburn, and P. Berrisford (2008), A new Rossby wave-breaking interpretation of the North Atlantic Oscillation, *J. Atmos. Sci.*, *65*, 609–626, doi:10.1175/2007JAS2347.1.
- Zhu, Y., and R. E. Newell (1998), A proposed algorithm for moisture fluxes from atmospheric rivers, *Mon. Weather Rev.*, *126*, 725–735, doi:10.1175/1520-0493(1998)126<0725:APAFMF>2.0.CO;2.